Materials Characterization 124 (2017) 171–181

Contents lists available at ScienceDirect

Materials Characterization

journal homepage: www.elsevier.com/locate/matchar

Microstructure of as-cast single and twin roller melt-spun Ni_2MnGa ribbons

G. Pozo-López [a,b,c,*], A.M. Condó [c,d,e], L.M. Fabietti [a,b,c], E. Winkler [c,d,e], N. Haberkorn [c,d], S.E. Urreta [a]

[a] Facultad de Matemática, Astronomía y Física, Universidad Nacional de Córdoba, Ciudad Universitaria, 5000 Córdoba, Argentina
[b] Instituto de Física Enrique Gaviola, CONICET, Argentina
[c] Consejo Nacional de Investigaciones Científicas y Técnicas (CONICET), Argentina
[d] Centro Atómico Bariloche, Comisión Nacional de Energía Atómica, Av. Bustillo 9500, 8400 San Carlos de Bariloche, Argentina
[e] Instituto Balseiro, Universidad Nacional de Cuyo, Av. Bustillo 9500, 8400 San Carlos de Bariloche, Argentina

ARTICLE INFO

Article history:
Received 17 November 2016
Received in revised form 17 December 2016
Accepted 22 December 2016
Available online 24 December 2016

Keywords:
Shape–memory alloys
Magnetic properties
Martensitic transformation
Rapid solidification
Microstructure
Transmission electron microscopy

ABSTRACT

Stoichiometric Ni_2MnGa alloys are processed by two rapid solidification techniques – single-roller (SR) and twin-roller (TR) melt spinning – and the resulting microstructures and magnetic properties determined. Samples processed at tangential wheel speeds of 10 m/s (V10) and 15 m/s (V15) are studied in the as-cast condition to analyze the influence of the production methods on the microstructure. Important aspects like the resulting phases, their crystallographic texture, magnetic properties, martensitic transformation temperatures and Curie temperatures are compared. In addition, the magnetization mechanism involving twin boundary motion is explored. Our results indicate that the TR method provides lower cooling rates, thicker samples, higher internal stresses and larger MnS precipitates. However, the quenching rate is mainly determined by the tangential wheel velocity. TR samples also exhibit [100] texture normal to the ribbon plane but in a lesser extent than SR ribbons. Martensitic transformation temperatures are higher in samples V15 (~150 K) than in V10 (~100 K), with no clear difference between the SR and TR modes. This behavior is explained by considering distinct degrees of disorder in the $L2_1$ austenite phase resulting from quenching. The hysteresis of the transformation, defined as the difference $A_f - M_S$, takes similar values in the four samples analyzed. Pre-martensitic transformation temperatures are also slightly higher in samples V15, (230 ± 3) K, than in samples V10, (222 ± 3) K, as the magnitude of the Hopkinson effect, in good agreement with a higher residual stress level in TR ribbons. In the martensitic state, all ribbons exhibit hysteresis loops characteristic of a magnetization mechanism involving twin boundary motion. The switching magnetic fields for the onset of Type I twin boundary motion result between 220 mT and 365 mT, values equivalent to twinning stresses of about 1 MPa. It is concluded that both procedures, SR and TR melt spinning, provide microstructures favoring magnetic field induced twin variant reorientation.

1. Introduction

During recent decades Ni-Mn-Ga Heusler-type alloys have emerged as a promising new class of smart materials due to the multifunctional properties they exhibit: magnetic shape memory effects [1–3], superelasticity [4], magnetoresistance [5,6] and magnetocaloric effects [7–11]. These alloys, with great potential for applications in magnetic sensing, actuation and magnetic refrigeration, combine the properties of ferromagnetism with those of a thermoelastic martensitic transformation. In this sense, the giant deformation observed under an external applied field, with the associated magnetic-shape-memory effect, is attributed to either the reversible field-induced austenite to martensite transformation [12], or the magnetic field-induced rearrangement (MIR) of martensitic variants via twin boundary motion, without any phase transition [1,13,14].

The phase transformation sequence in Ni-Mn-Ga alloys is actually quite complex; depending on the alloy chemical composition and thermal history, different transformations may proceed. On cooling from the melt, the Ni_2MnGa stoichiometric compound is formed as a partially ordered (with respect to the nickel sublattice) B2 phase. The subsequent ordering of Mn and Ga atoms occurs below 1071 K with the formation of the Heusler phase (austenite) with cubic $L2_1$ structure [15,16]. In this austenitic phase, Ni ions occupy the corner sites of a body-centered-cubic structure, while Mn and Ga ions occupy alternate body-center sites [17]. In some near-stoichiometric alloys, prior to the martensitic transformation at low temperatures, a weak first order transformation occurs from the austenitic phase into a micro-modulated pre-martensitic phase, as a result of a soft $1/3[110]TA_2$ phonon mode condensation [18,19]. The martensitic transformation in Ni-Mn-Ga alloys may result in several martensites: five-layered (5 M) [2,20] or seven-layered

* Corresponding author at: Facultad de Matemática, Astronomía y Física, Universidad Nacional de Córdoba, Ciudad Universitaria, 5000 Córdoba, Argentina.
E-mail address: gpozo@famaf.unc.edu.ar (G. Pozo-López).

http://dx.doi.org/10.1016/j.matchar.2016.12.020
1044-5803/

(7 M) [3,20] modulated monoclinic martensitic structure, or a non-modulated (NM) tetragonal martensite structure [20,21]. In addition, inter-martensitic transformations also exist in alloys with martensitic transformation temperatures near or higher than room temperature. These are first-order phase transitions between different martensitic structures; typical transformation paths of inter-martensitic transformations on cooling were reported as 5 M–7 M-NM or 7 M-NM [22–25], being the final NM martensite the most stable. Recent studies also demonstrate that in many cases austenite can transform into coexisting multiple martensites with different structures [26]. At $T_C = 376$ K [16] the Ni_2MnGa alloy exhibits a para-to-ferro-magnetic transition; since the martensitic transition temperature is lower than the Curie point, martensitic transformation occurs between ferromagnetic phases. In contrast to the martensitic transformation temperatures, the Curie temperatures of off-stoichiometric Ni-Mn-Ga alloys are less sensitive to the chemical composition, having a value of around 370 K for a wide composition range [27].

So far, magnetic-field-induced strains of approximately 6% and 10% have been reported in Ni-Mn-Ga single crystals of 5 M [2,13] and 7 M [3] martensites, respectively, but only negligible MFIS has been observed in NM martensite (not larger than ~0.1% [28]). Due to the high fabrication cost of single-crystals and in order to minimize actuators size and ac eddy-current losses, research was also directed towards polycrystalline materials. Although the observed MFIS in polycrystalline samples is almost zero [29], attempts have been made to improve the magnetic field induced strain producing the alloys as thin films, ribbons, particles and foams [30]. As already mentioned, microstructures and phase transition sequences in Ni-Mn-Ga alloys strongly depend on their chemical composition. In addition, other structural and magnetic properties such as crystal type, transition temperatures, and/or internal stresses can be further tuned by the whole preparation route [31].

In recent years, the melt-spinning technique has been successfully adopted as an effective single-step process to produce nearly homogeneous single-phase textured ribbons [30,32–36]. The high internal stresses induced in the ribbons result in preferentially oriented textures that favor large transition-induced strain and MFIS. Melt-spun polycrystalline Ni-Mn-Ga ribbons exhibit in the as-cast condition, and even after annealing at temperatures below 773 K, a marked step in the martensite $M(H)$ hysteresis loops [30], which has been attributed to magnetic-field-induced twin boundary motion (MFITBM) [14] in the particular scenario of quenched-in internal stresses, built up during the rapid solidification process.

Polycrystalline melt-spun samples have been processed by single [30] and double [36] melt-spinning techniques; in both cases the resulting ribbons exhibit relatively large contributions to the total polarization associated to a mechanism of field-induced twin boundary motion. In both processing methods, the main variables are the melt flow rate, largely controlled by the nozzle diameter and the ejection argon overpressure, the melt temperature and the rolling wheel tangential speed. In the case of twin-roller melt spinning, a second wheel is in contact with the melt, providing a symmetric heat extraction pattern, and a new variable becomes important: the resistance to separate the rolling wheels, known as the separating force [37]. This resistance is provided by calibrated springs forcing the wheels together. This variable becomes crucial to determine the ribbon thickness, the heat extraction rate and the actual cooling speed, and also the residual internal stress level. These internal stresses also increase the critical field required for MIR.

Optimal microstructure to observe 'recoverable' MIR effect in melt-spun ribbons, requires columnar grains of the $L2_1$ ordered austenitic phase, developing along the ribbon thickness, with the [100] crystalline direction perpendicular to the ribbon plane. An effective long-range internal tensile stress directed along the ribbon length is also necessary to promote a single (or few) variant/s in the martensitic phase after cooling, and a back-stress acting as a restoring force. Defects like compositional inhomogeneities, localized chemical disorder, small precipitates, dislocations and other randomly distributed local defects are pinning points for twin boundaries and hinder their motion, so they must all be minimized.

It is then of interest to investigate in what extent the single and double roll procedures provide the optimal conditions for MIR.

Considering the high sensitivity of the actual solidification conditions to a large number of variables, any comparison of performances between the single and twin roller procedures must be made in as similar as possible devices. In this sense, the melt spinning facility in our laboratory works in the two modes, single and double roller, shearing all other dispositive as oven, crucible, ejecting system and cooling cylinders.

This article reports on the microstructure, transformation temperatures, magnetism and ferroelastic behavior of Ni_2MnGa alloys, processed by two rapid solidification techniques: single-roller and twin-roller melt spinning. For each one of these conditions two different tangential wheel speeds are considered. Samples are studied in the as-cast condition to analyze the influence of the production methods on the microstructure; aspects like phases, crystallographic texture, magnetic properties, martensitic transformation temperatures and Curie temperatures of the alloys are compared. In addition, the magnetization mechanism involving MIR in each structure, which is at the origin of magnetic field induced strain, is explored. All the properties are also compared with the ones reported in literature for Ni_2MnGa bulk alloys, produced by traditional methods.

2. Materials and Methods

A master alloy of nominal composition Ni_2MnGa was prepared by arc melting 99.9% pure Ni (Strem Chemicals), 99.995% pure Mn (Johnson Matthey) and 99.99% pure Ga (Strem Chemicals). The small ingots so obtained (about 5 g) were re-melted four times to promote a homogeneous distribution of the components. All these procedures were conducted under a Zr gettered Ar atmosphere, with a weight loss during arc melting less than 0.6%. Ingots were melted under argon atmosphere in a quartz crucible with a circular 1 mm diameter nozzle by induction heating. The molten alloy (~1573 K) was evacuated by a positive argon pressure onto one (single-roller melt-spinning technique: SR) or two (twin-roller melt-spinning technique: TR) 5 cm diameter copper wheel/s, coated with a thick chromium layer. Casting was performed at two different tangential wheel speeds: 10 m/s and 15 m/s (samples V10 and V15, respectively); as-quenched ribbons were flakes of about 1.7–2.5 mm wide and 50–80 μm thick, as shown in Table 1. As expected, ribbons are thinner in SR samples than in the TR ones and thickness tends to reduce as the tangential wheel speed increases.

Ribbon morphology was examined in a Leica DMRM optical microscope. Fig. 1 shows the typical morphology of the surfaces solidified in contact with the wheel (CS: contact surface, SR or TR) and solidified at air (FS: free surface, SR). For samples produced by the twin-roller melt-spinning technique, no differences were observed between the ribbon faces, indicating symmetric solidification conditions.

The resulting microstructures were characterized by X-ray diffraction (XRD), scanning electron microscopy (SEM) and transmission electron microscopy (TEM). Room temperature X-ray diffraction profiles were recorded in a Philips PW 3830 diffractometer in the 2θ range from 20° to 100°, in Bragg-Brentano configuration, using Cu $K\alpha$

Table 1
Mean thickness t and average width w of the ribbons V10 SR, V10 TR, V15 SR and V15 TR.

Sample	V10 SR	V10 TR	V15 SR	V15 TR
t [μm]	60 ± 5	80 ± 5	50 ± 5	70 ± 5
w [mm]	2.2 ± 0.4	2.5 ± 0.5	1.8 ± 0.5	1.7 ± 0.5

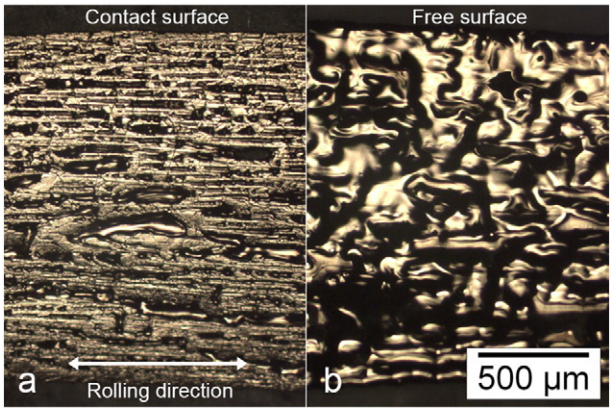

Fig. 1. Optical micrographs of a ribbon showing the typical morphology of the surfaces (a) solidified in contact with the wheel (CS: contact surface) and (b) solidified at air (FS: free surface). Both images correspond to a V15 SR ribbon and the rolling direction is evident in the contact surface.

radiation ($\lambda = 1.5418$ Å). A Philips 515 scanning electron microscope was used to image the ribbons fracture surfaces. Samples observed by TEM were thin foils prepared by twin-jet electropolishing with a 20% HNO_3 (nitric acid)/80% pro-analysis methanol electrolyte, at 12 V and 258 K. Transmission electron microscopy observations and selected area diffraction patterns were performed in a Philips CM200UT microscope, operating at 200 kV and equipped with energy-dispersive X-ray spectroscopy (EDS) facility.

Magnetic measurements were performed in a Quantum Design SQUID magnetometer, in 6 mm long as-cast ribbons with the applied field parallel to the sample length. Magnetization as a function of temperature curves $M(T)$ were measured in the temperature range 5–300 K, under an applied field of 2 mT. Magnetization isotherms $M(H)$ curves were recorded at selected temperatures within that range, up to a maximum field of 1.5 T. Curie temperatures were estimated from magnetization vs. temperature curves measured in a Faraday balance, in the 290 K - 400 K temperature range, at a rate of 0.7 K/min.

Additionally, electrical transport was measured with the conventional four-probe geometry between room temperature and 10 K.

3. Results and Discussion

3.1. Scanning Electron Microscopy

Fig. 2 shows typical SEM images of the ribbons' cross sections. In samples produced by single-roller melt-spinning (SR), small equiaxed grains are found near the surface in contact with the wheel, as well as long columnar grains (2–8 μm wide) grown-up through the whole ribbon thickness. On the other hand, small equiaxed grains are observed on both surfaces of TR melt-spun samples (both solidified in contact with a wheel) but columnar grains in the central zone are coarser, with widely distributed orientations as compared to SR ribbons. These features indicate that, higher rates of heat removal during the process of rapid solidification enhance directional grain growth [38].

3.2. X-ray Diffraction Analysis

Room temperature XRD patterns of the as-cast alloys, solidified at different rates, are shown in Fig. 3. For SR samples, both surfaces of the ribbons (CS and FS) were exposed to the incident radiation. Diffractograms were indexed according to a $L2_1$ crystal structure [16,39]. As can be seen, only the (200) superlattice reflection, indicative of the nearest-neighbor B2 ordering, is visible in all samples. The (111) superlattice reflection, corresponding to the next-nearest-neighbor $L2_1$ ordering, is only observed in sample V15TR. Secondary phases were not detected; the diffraction peak denoted with letter "T" corresponds to the double-coated tape used to paste the ribbons to the XRD specimen holder.

The lattice constant a of the $L2_1$ austenitic phase was calculated by fitting to the structural reflections 220, 400, 422 and 440 a Pearson VII profile; corrected values of 2θ were used by considering the zero shift effect as described in [40]. The resulting values – listed in Table 2 – are indistinguishable within experimental errors and coincide pretty well with the value $a_0 = 5.825$ Å reported by Webster et al. [16] and tabulated in card ICSD #103803.

As already reported in [30,35,36] melt-spun ribbons exhibit texture, with the [100] crystalline direction almost perpendicular to the ribbon plane. In fact, [100] preferred texture about 5° tilted from the ribbon normal has been reported in SR samples [35]. This anisotropy is more

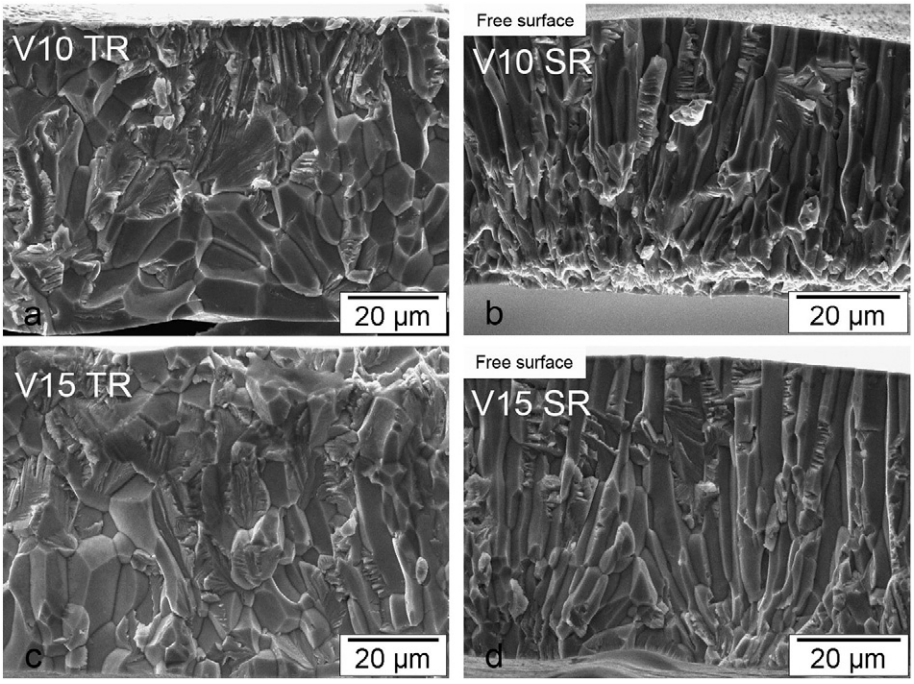

Fig. 2. SEM images of the cross sections of V10 (a and b) and V15 (c and d) ribbons produced by twin-roller (a and c) and single-roller (b and d) melt-spinning techniques.

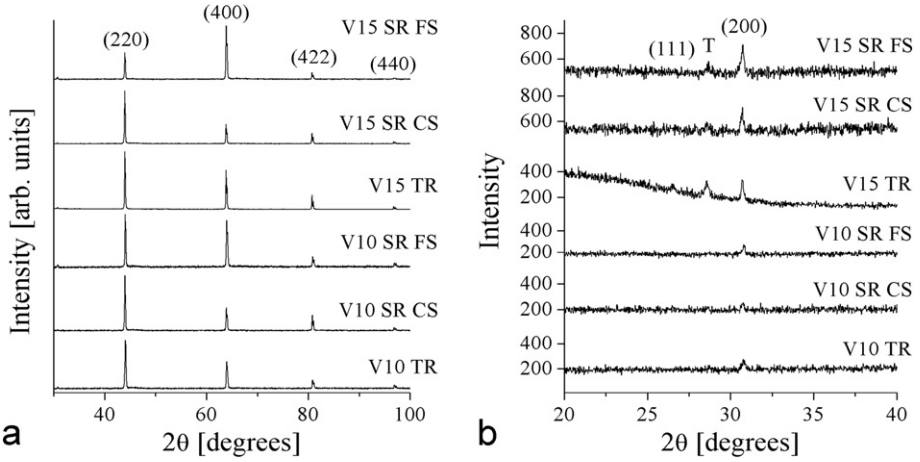

Fig. 3. (a) Room temperature X-ray diffraction patterns of the as-cast ribbons. Relative intensities of structural reflections from the ordered $L2_1$ cubic austenite structure can be observed. (b) Low angle detail of (a) showing (111) and (200) superlattice diffraction lines from $L2_1$ austenite phase. Letter "T" denotes the diffraction peak of the double-coated tape used to paste the ribbons to the XRD specimen holder.

notorious in SR samples (particularly near the free surface, FS). Diffraction peak intensity ratios I_{400}/I_{220} for all the samples studied are listed in Table 2; the reference relative intensity value corresponding to Ni_2MnGa (card ICSD #103803) is 0.15. This confirms that this texture is also present in our TR samples.

XRD and SEM results indicate that SR samples exhibit longer columnar grains, with the growing [100] direction highly oriented perpendicular to the ribbon plane, which is a necessary condition to obtain only few variants in the martensitic phase after cooling. The other one is to obtain a convenient long range stress distribution [11,35] which is known to exist in SR ribbons but not "a priori" expected in TR ones. As discussed by Wang et al. [30], the crystallographic texture in the austenite phase, [100] direction perpendicular to the ribbon plane, and the quenched-in stress (tensile along ribbon length) promote variant selection on the martensitic transformation. For a tensile stress ($\sigma > 0$), the negative magnetoelastic coupling in the martensite makes the magnetic moment vectors to align normally to the stress. Then, under such tensile stress only those variants whose hard magnetization direction (a axis) is parallel to the stress direction (ribbon plane) are selected.

3.3. Transmission Electron Microscopy

Energy-dispersive X-ray spectroscopy (EDS) analysis on the melt-spun ribbons confirmed the stoichiometric composition Ni_2MnGa in all samples, with a quite narrow dispersion (<1 at.%) around the nominal composition.

Conventional selected area electron-diffraction patterns (SAEDP) ratified the $L2_1$ austenite crystalline structure in all the samples; Fig. 4 shows the electron diffraction [112] zone axis pattern for sample V10 SR, in which 111-type Heusler superlattice diffraction spots reveal the $L2_1$ atomic order in the ribbons. The [100] orientation was mainly observed in accordance with XRD results.

TEM bright field images of samples in the austenitic phase are displayed in Fig. 5. Small pores and thinner circular regions are observable, due to preferential etching around former precipitates. Dislocations with helical configuration are found around some precipitates in all the samples (see Fig. 5.b, sample V10 TR). These dislocations were already observed by us in twin-roller melt-spun Ni_2MnGa ribbons [36] and by Serrano et al. [41] in quenched β-CuZnAlNi shape memory alloys with the same $L2_1$ structure. These latter authors propose that they form by vacancy condensation.

Precipitate diameter, d_P, is in the range between 10 nm and 100 nm. As their volume density is relatively small, no statistically significant histograms could be built. Instead, the arithmetic means over 100 particles, with the corresponding standard deviation, are considered. These mean values are listed in Table 2.

A number of studies have demonstrated that precipitates can have a strong effect on twin boundary motion [42] by acting as obstacles, characterized by their energy and spatial distributions. The precipitates in our samples have different mean sizes, being larger in TR samples (30–60 nm), than in SR ones (15–30 nm), however, no rigorous correlation between their mean size and the critical field for twin boundaries motion could be well established as will be shown below.

Fine probe EDS microanalysis (Fig. 6.a) indicated that these precipitates contain Mn and S (sulphur is the main impurity in the Mn precursor used) in their composition. Fig. 6.b shows a 200 dark field micrograph of a ~40 nm diameter precipitate exhibiting Moiré fringes (sample V10 SR). In the upper side of the image, the corresponding electron diffraction pattern evidences extra spots belonging to the precipitate. The nearness between the precipitate P and 200 austenitic matrix reflections produces the observed Moiré fringes. The ratio between

Table 2
Lattice constant a and intensity ratio I_{400}/I_{220} of the high temperature austenitic phase, obtained from XRD data. Card ICSD #103803 indicates $a_0 = 5.825$ Å at room temperature and $I_{400}/I_{220} = 0.15$. The mean precipitate size d_P, obtained from TEM images, is also listed.

	V10 SR		V10 TR	V15 SR		V15 TR
Sample	FS	CS		FS	CS	
$a \pm 0.002$ [Å]	5.823	5.824	5.825	5.825	5.827	5.828
I_{400}/I_{220}	0.88	0.48	0.73	2.25	0.43	0.72
d_P [nm]	15 ± 10		60 ± 20	30 ± 10		30 ± 15

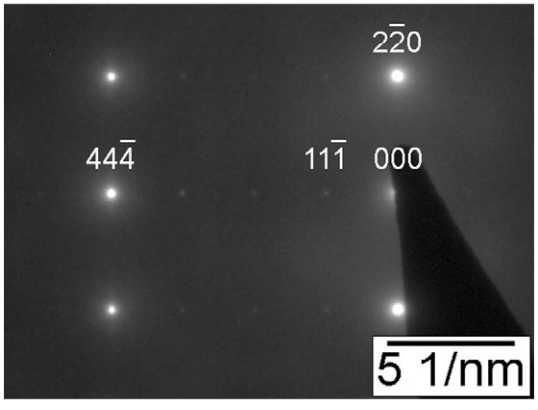

Fig. 4. Electron diffraction [112] zone axis pattern (sample V10 SR) corresponding to the $L2_1$ structure.

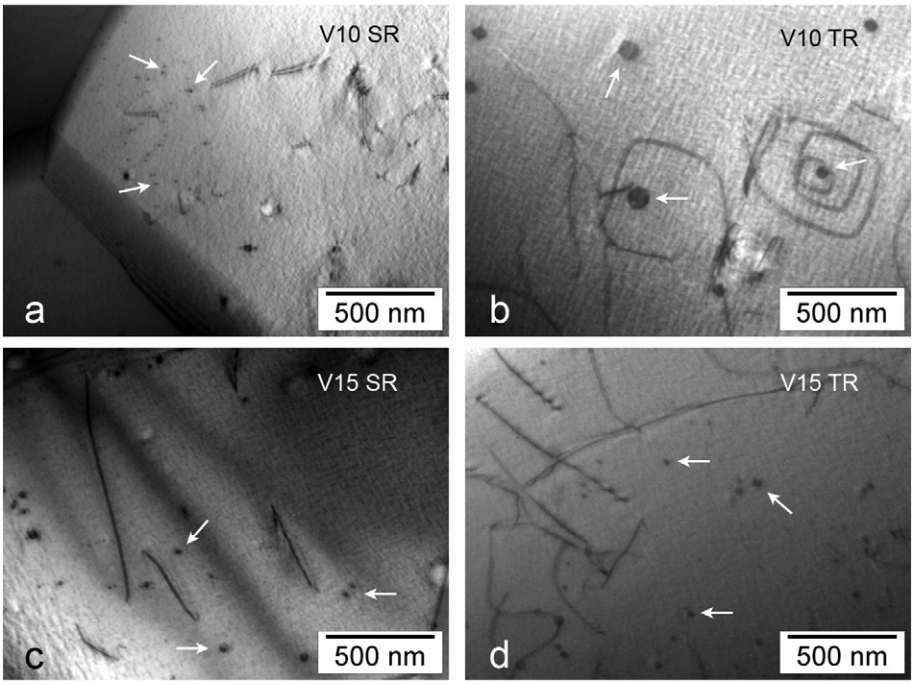

Fig. 5. TEM bright field (BF) micrographs showing MnS precipitates (some of them indicated with arrows) and dislocations inside the grains. Helical dislocations shown in V10 TR are vacancy sinks [41].

the interplanar distances in the precipitate and in the austenite matrix d_P / d_{a200} equals 0.90. In this sense, taking into account composition results and assuming a cubic crystal structure for the second phase, a lattice parameter a_P of about 5.2 Å was calculated for the precipitates, considering the interplanar distances ratios measured by TEM and the austenite lattice parameters obtained by XRD studies. This value is very close to the lattice parameter $a_{MnS} = 5.224$ Å tabulated for the stoichiometric α-MnS phase (PDF # 00-006-0518), the only stable compound in the Mn—S system, with NaCl-type structure [43]. Fig. 6.c displays a bright field image of a group of precipitates and Fig. 6.d the dark field image corresponding to the precipitates reflection g = 200. Comparing the bright and dark field images, it is evident that all the precipitates are diffracting indicating a definite orientation relationship with the matrix, as was previously observed [36]. Even more, under two-beam condition, the precipitates show the typical butterfly diffraction contrast (Ashby-Brown contrast [44]) of coherent precipitates due to lattice mismatch with the matrix. This fact is exemplified in Fig. 6.e, which shows a bright field micrograph taken under two beam condition with the austenite g = 200. With these results, a NaCl-type structure with orientation relationship $<100>_P // <100>_a$ is assumed for the precipitates, and the corresponding reflection P in Fig. 6.b is indexed as 200.

3.4. Martensitic Transformation Temperatures

Magnetization versus temperature curves were measured in the range between 4 K and 300 K, where the martensitic transformation is expected to take place. Samples were first zero-field-cooled to 4 K (without measurement), then field-heated (ZFC) to room temperature and field cooled (FC) back to 4 K under a constant applied field of 2 mT. The resulting thermomagnetic curves for the four samples investigated are shown in Fig. 7. On cooling from room temperature, the abrupt change in the magnetization value indicates the transformation starts from the high temperature Heusler austenitic phase (A) to the martensitic phase (M). During heating, the phase transformation reverses showing temperature hysteresis. Martensite start and finish temperatures (M_S, M_f) and austenite start and finish temperatures (A_S, A_f) are also indicated in Fig. 7, together with a graphic illustrating the procedure to determine them. A summary of these characteristic temperatures is presented in Table 3.

Austenitic and martensitic phases show distinct magnetic characteristics. The cubic austenite is magnetically soft, with low anisotropy energy, and exhibits low hysteresis, coercivity and remanence values. On the other hand, martensite presents a relatively large uniaxial anisotropy. These differences allow detecting the martensitic transformation during field cooling the material through its transition temperature. A significant drop in the magnetic moment is observed as the transformation progresses indicating that the magnetic anisotropy increases and the number of easy axes closely aligned with the applied field direction [16,45] reduces.

Transformation temperatures and the respective hysteresis can also be detected studying the temperature dependence of electrical resistance. Fig. 8 shows a typical (room temperature normalized) resistance vs. temperature curve, measured in sample V15 TR. The corresponding martensite and austenite start and finish temperatures are also listed in Table 3. A relatively good agreement is found between these values and the ones obtained from magnetization vs. temperature measurements, but they are lower than those registered for bulk Ni_2MnGa alloys ($M_S = 202$ K [16]). Lower transformation temperatures, as compared to that of bulk samples with the same composition, were already measured in other Ni-Mn-Ga melt-spun ribbons [34,36,46–48]. The observed reduction in the martensitic transformation temperatures can be related to internal stresses and disorder, built up in the rapid solidification process, and to smaller grain size. Melt-spun ribbons with grain refinement have a larger amount of grain boundaries, in which the short-range atomic chemical disorder is increased. This disorder enhances the resistance to the transformation and depresses the martensitic transformation temperature [32].

Martensite and austenite start temperatures are higher for the ribbons quenched at 15 m/s (SR and TR); for a given wheel speed, no significant differences are observed between the characteristic temperatures of the SR and TR melt-spun samples. The hysteresis of the transformation, defined as the difference $A_f - M_S$, takes similar values for the four samples analyzed, resulting in an average value of 34 ± 3 K. The hysteresis value can be related to the nature of the martensitic transformation and to the sample microstructure [49].

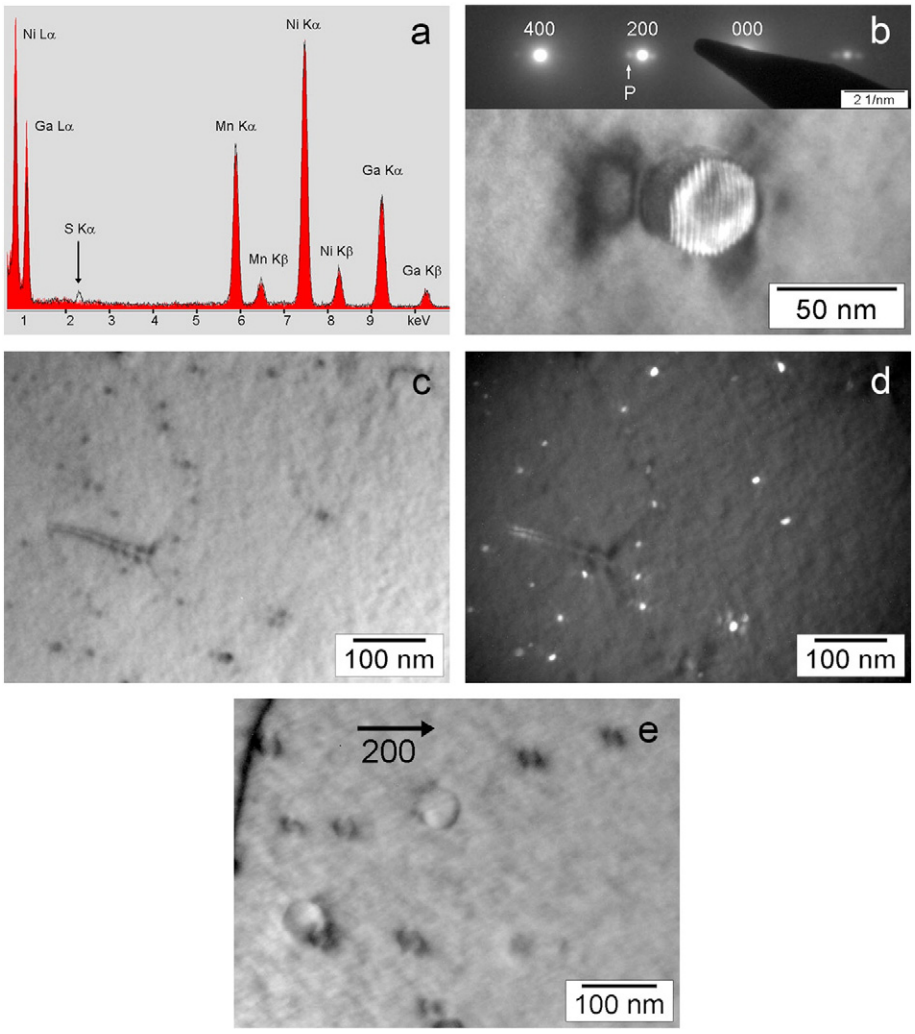

Fig. 6. (a) EDS from a precipitate (black line) compared to the Ni-Mn-Ga matrix (full red). In the precipitate, the S Kα peak is evident and a small increment in the Mn Kα peak is observed (sample V15 SR). (b) 200 dark field micrograph of a ~40 nm diameter precipitate, exhibiting Moiré fringes (sample V10 SR). In the upper side of the image, the corresponding electron diffraction pattern, presents extra spots belonging to the precipitates (P). Non indexed reflections correspond to double diffraction. (c) Bright field micrograph of V10 SR sample and (d) the corresponding dark field image with reflection g = 200. (e) Coherent precipitates with butterfly diffraction contrast can be observed in this bright field image obtained close to the two beam condition with g = 200. The direction of g is indicated in the figure (sample V15 TR).

The increase of M_S with the tangential wheel velocity may be rationalized by considering that the value of M_S strongly depends on the degree of order in the parent phase. When NiMnGa alloys solidify, the atomic structure follows the sequence: liquid → disordered B2 phase → ordered $L2_1$ phase. For Ni_2MnGa the transition temperatures are $T_1 = 1383$ K and $T_2 = 1071$ K, respectively [50]. The order-disorder transformation cannot be avoided; however, depending on the cooling and quenching conditions [51], different grades of order may exist in the resulting $L2_1$ phase. In addition, there is a significant difference if a NiMnGa alloy is quenched from temperatures above or below T_2. If the sample is quenched from temperatures below T_2 (from the ordered $L2_1$ phase field), increasing the quenching rate also increases the retained disorder in the austenitic phase, causing the temperature M_S to decrease, as found in our previous work [36]. Now, if the sample is quenched from a higher temperature, above T_2, the increment in the vacancy concentration helps the ordering process during the quench [52], leading to an increased retained order and the consequent increase in M_S. Solidification is a continuous cooling method; in particular, in a rapid solidification event, the diffusion time is similar to that of the quenching process. We do not know at what temperature the microstructure actually freezes but in the present work, M_S for the V10 condition is below that obtained for V10 in [36]. Besides, the difference between the X-ray diffraction patterns in the previous and the present work points out a higher disorder in the new samples because the order diffraction lines are not detected as they were in the former case. Both results are an indication that the cooling rate is now higher than in [36], so it is likely that the frozen microstructure in V15 corresponds to a temperature higher than T_2 causing the M_S to increase and not to decrease as before.

Another parameter characterizing the transformation is the so-called equilibrium temperature T_0. Kaufman and Cohen [53] first introduced the concept of T_0 as the temperature at which the chemical Gibbs free energy of the parent and martensitic phases are equal. Thus, at T_0 they are thermodynamically in (metastable) equilibrium, whereas at lower temperatures, the martensitic phase is stable. For several thermoelastic transformations, it may be assumed that it is half way between M_S and A_f temperatures leading to:

$$T_0 \approx \frac{M_S + A_f}{2}.$$

The resulting values for T_0, estimated from magnetization and resistance measurements, are included in Table 3; the equilibrium temperature is higher in samples cooled at higher wheel speeds and it is no sensitive to the particular (SR or TR) cooling mode.

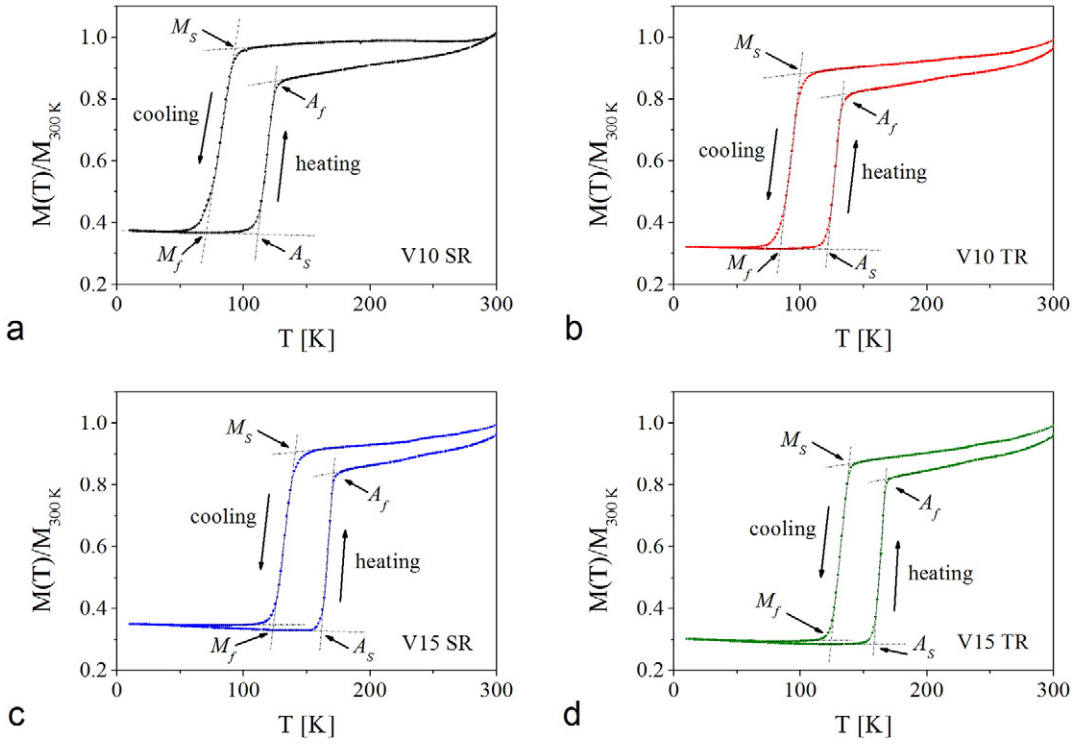

Fig. 7. Normalized magnetization vs. temperature curves measured under a constant field of 2mT: (a) sample V10 SR, (b) sample V10 TR, (c) sample V15 SR and (d) sample V15 TR. Martensitic and austenitic transformation temperatures are shown.

In addition to the martensitic transformation, an extra feature is observed in the electrical resistance curve at temperatures above the martensitic transition, which is associated with the formation of an intermediate or pre-martensitic (PM) phase. This pre-martensitic transformation has been detected in $Ni_{2+x+y}Mn_{1-x}Ga_{1-y}$ alloys with relatively small deviations from stoichiometry and martensitic transformation temperatures lower than 270 K [18]. It is a weak first order transformation [54] which, for the stoichiometric composition Ni_2MnGa with martensitic transformation temperatures around 200–220 K, occurs near 260 K [15,17,55]. Pre-martensitic transformation temperatures (T_{PM}) obtained in this work are a bit lower (~225 K) than this latter value, but are comparable to the one obtained by Chernenko et al. [18] for a polycrystalline alloy with the same electron concentration (electron to atom ratio $e/a = 7.5$): $M_S = 113$ K, $T_{PM} = 224$ K. Gonzàlez-Comas et al. [56] found a similar value of about 230 K in a single crystal with composition very close to the stoichiometric one, and Sánchez-Alarcos et al. [57] measured a $T_{PM} = 213$ K, in a near stoichiometric Ni_2MnGa polycrystalline sample with low transition temperatures (M_S ~ 100 K).

Table 3
Martensitic and austenitic transformation temperatures in melt-spun samples Ni_2MnGa determined from magnetization vs. temperature curves (J) and electrical resistance measurements (R).

Sample	V10 SR	V10 TR	V15 SR	V15 TR
${}_JM_S$ [K]	93 ± 3	100 ± 3	141 ± 3	138 ± 3
${}_RM_S$ [K]	95 ± 3	91 ± 3	143 ± 3	124 ± 3
${}_JM_f$ [K]	71 ± 3	84 ± 3	123 ± 3	124 ± 3
${}_RM_f$ [K]	74 ± 3	65 ± 3	118 ± 3	102 ± 3
${}_JA_S$ [K]	111 ± 3	121 ± 3	161 ± 3	158 ± 3
${}_RA_S$ [K]	118 ± 3	114 ± 3	149 ± 3	152 ± 3
${}_JA_f$ [K]	125 ± 3	133 ± 3	171 ± 3	167 ± 3
${}_RA_f$ [K]	130 ± 3	121 ± 3	176 ± 3	164 ± 3
${}_JT_0$ [K]	109 ± 6	116 ± 6	156 ± 6	153 ± 6
${}_RT_0$ [K]	113 ± 6	103 ± 6	159 ± 6	146 ± 6
${}_RT_{PM}$ [K]	222 ± 3	221 ± 3	230 ± 3	228 ± 3

3.5. Magnetic Properties

The magnetization versus temperature curves measured during heating in the range 290 K–400 K, under two external fields, are shown in Fig. 9, for the four alloys investigated. Curie temperatures were taken as those where the dM/dT warming curves reach a minimum. The resulting values, quoted in Table 4, are indistinguishable within experimental errors, for the two low external magnetic fields employed, and relatively close to those reported for Ni_2MnGa bulk samples [15,16]. As can be seen, Curie temperatures do not depend on the sample microstructure as long as the alloy composition remains unchanged.

A Hopkinson peak [58] is clearly observed in all the $M(T)$ curves: as temperature rises magnetization first increases, goes through a

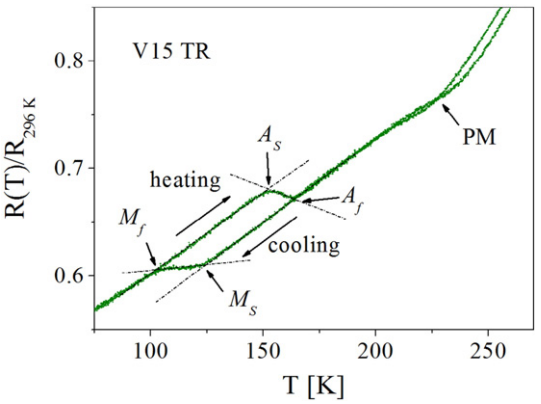

Fig. 8. Typical normalized resistance R(T)/R(296 K) vs. temperature curve showing a pre-martensitic (PM) and the martensitic transformation temperatures. The graphical procedure used to determine the transformation temperatures is illustrated. M_S: martensite start temperature, M_f: martensite finish temperature, A_S: austenite start temperature, A_f: austenite finish temperature and T_{PM}: pre-martensitic transformation temperature.

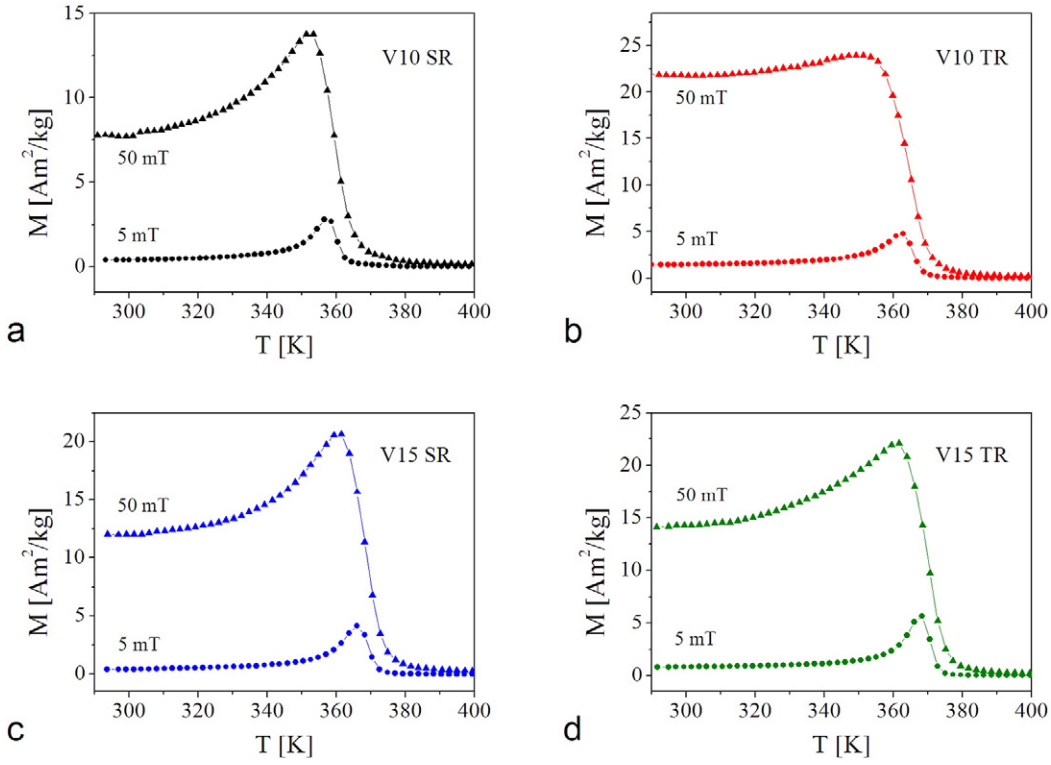

Fig. 9. Thermomagnetic heating curves, measured at 5 mT and 50 mT between 290 K and 400 K for samples V10 SR (a), V10 TR (b), V15 SR (c) and V15 TR (d). A Hopkinson maximum is observed in all the $M(T)$ curves.

maximum just below the Curie point, to abruptly decrease at T_C. The Hopkinson effect is related to the fact that the crystal anisotropy and magnetostriction both vanish below T_C, before the sample becomes paramagnetic. Then, in a given temperature interval the spins easily rotate to the applied field direction, leading to the magnetization increment observed. In this condition the effectiveness of quenched-in residual microstresses and easy axis distributions vanish. Under an applied field of 5 mT, the magnitude of the Hopkinson effect is larger in twin-roller melt-spun samples (see Fig. 10) in good agreement with the higher residual stress level expected in these ribbons, as compared to SR ones.

Fig. 11 illustrates typical hysteresis loops corresponding to the austenitic (Fig. 11.a) and martensitic (Fig. 11.b) phases in samples V10SR, where critical fields are indicated. The upper branches of the isothermal hysteresis loops were measured at two different temperatures: one in the range of the high temperature austenitic phase and another one at low temperature, where the martensitic transformation is complete (Fig. 12). The corresponding differential susceptibility χ curves are shown in the insets of Fig. 12 for the four microstructures investigated. Abrupt slope changes appear on the $J(H)$ curves in the martensite phase, a behavior already observed in other Ni-Mn-Ga melt-spun ribbons [35,59]. It is worth to note that two distinct peaks are detected in the $\chi(H)$ plot during demagnetization of the martensitic phase from saturation; the first maximum (first step in the demagnetization curve) appears at a positive (first quadrant) internal field $\mu_0\chi H_{C1}$, while for increasing demagnetizing inverse fields, another step is observed at $\mu_0\chi H_{C2}$ of about −300 mT. These hysteresis loop features are completely reproduced during subsequent field cycles. The larger step has already been observed in $Ni_{51}Mn_{28.5}Ga_{20.5}$ polycrystalline ribbons, processed by single-roller melt-spinning [30,35] and was attributed to a magnetization mechanism involving twin boundary motion in the martensitic phase. These authors explain the phenomenon on the basis of the ribbon crystallographic texture and the internal stresses built up during quenching, which induce the cubic austenite to transform into a few variants of orthorhombic martensite during cooling. These quenched tensile stresses promote those twin variants with hard magnetization direction – *a* axis – parallel to the stress direction (ribbon plane) and the shortest *c* (easy) axis of the orthorhombic lattice normally aligned with the stress. In that way, the slope change in the martensite $J(H)$ curves would correspond to the onset of magnetic induced twin boundaries motion (MFITBM) in the preferentially oriented martensite. The restoring "force" leading to 'recoverable' twin boundary motion is proposed to be the grain-to-grain elastic energy stored in the polycrystalline ribbon.

Table 4
Curie temperatures T_C estimated from the dM/dT derivative of the $M(T)$ warming curve.

T_C [K]	V10 SR	V10 TR	V15 SR	V15 TR
H_{ap} = 5 mT	360 ± 3	365 ± 3	370 ± 3	371 ± 3
H_{ap} = 50 mT	359 ± 3	365 ± 3	368 ± 3	371 ± 3

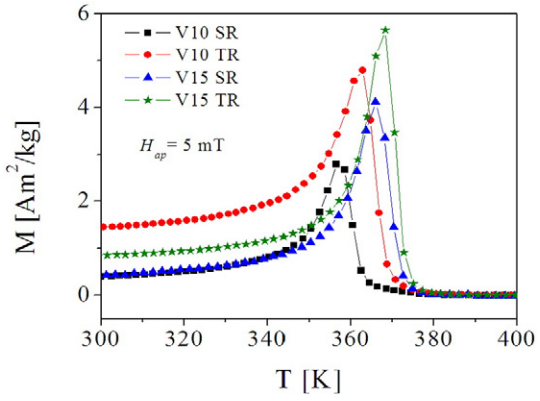

Fig. 10. Low field thermomagnetic curves measured during heating for the four samples investigated.

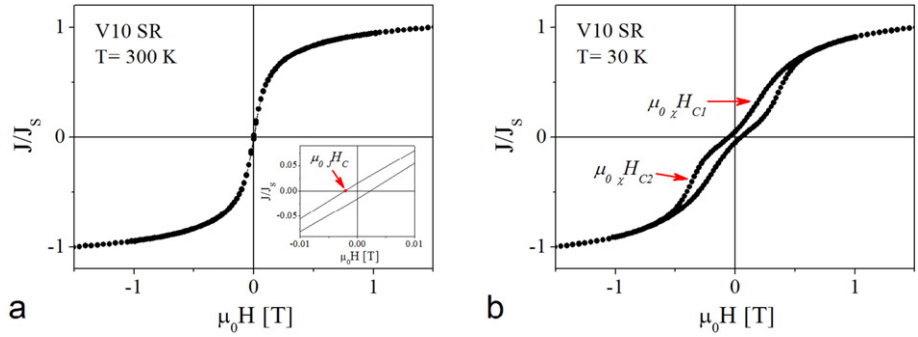

Fig. 11. Typical hysteresis loops corresponding to (a) the austenitic and (b) martensitic phases where critical fields are indicated.

Even when the nature of the martensitic phase is not unambiguously determined (no low temperature X-ray or neutron diffraction data is available) texture and quenched-in stresses present in our samples are similar to those found for modulate martensite. One necessary condition for MFITBM is a highly mobile twin boundary or interface between two differently oriented martensite variants (ferroelastic domains). In 10 M modulated martensite, two types of mobile twin boundaries (Type I and Type II) are observed with complex layered microstructures consisting of a hierarchy of twinning systems [60–63]. Then, the large peak in the $\chi(H)$ curve at $\mu_{0\chi}H_{C2}$ is likely to be related to the onset of Type I twin boundary motion, under the action of the applied magnetic field. The resulting values, between 220 mT and 365 mT, are consistent with reported switching fields of $\mu_0 H_{sw} \approx 0.3$ T [14] and $\mu_0 H_{sw} \approx 240$ mT [64], for the onset of Type I boundaries motion. This last field strength is equivalent to a twinning stress σ_{tw} of about 1 MPa. Unfortunately, the $\mu_{0\chi}H_{C2}$ values obtained could not be clearly correlated with the internal stress level, precipitate size or density or with the dislocation density in the samples.

On the other hand, it is not clear at present if the small peaking effect in $\chi(H)$ at $\mu_{0\chi}H_{C1}$, originates in demagnetizing effects alone and/or in any complex ferroelastic relaxation as the magnetic applied field reduces. The critical fields $\mu_{0\chi}H_C$ associated to the steps in the hysteresis loops of the martensitic phase are listed in Table 5.

4. Conclusions

Ni_2MnGa alloys are rapidly solidified by single-roller and twin-roller melt spinning at two different tangential wheel speeds. At room temperature and in the as-cast condition all ribbons are polycrystals of the austenitic phase with cubic $L2_1$ crystal structure. The influence of the production route on the microstructure and magnetic properties, especially the MFITBM, is evaluated.

Samples solidified in the single roller device (SR) are thinner and show more defined columnar grain structures and a more marked texture, with [100] direction perpendicular to the ribbon plane, indicating higher cooling rates and highly directional heat extraction.

Coherent precipitates, associated to sulphur traces in the manganese precursor, are found in all the samples. They are identified as the α-MnS stable compound in the Mn—S system with NaCl-type structure. Their diameters, d_P, are in the range between 10 nm and 100 nm and they exhibit orientation relationship $<100>_P$ // $<100>_a$ with the matrix and a lattice parameter a_P of about 5.2 Å. These coherent precipitates are larger in TR samples (30–60 nm) than in SR ones (15–30 nm) and no rigorous correlation between their mean size and the critical field for twin boundaries motion could be well established.

Transformation temperatures are lower than in bulk samples with the same composition due to internal stresses, built up during

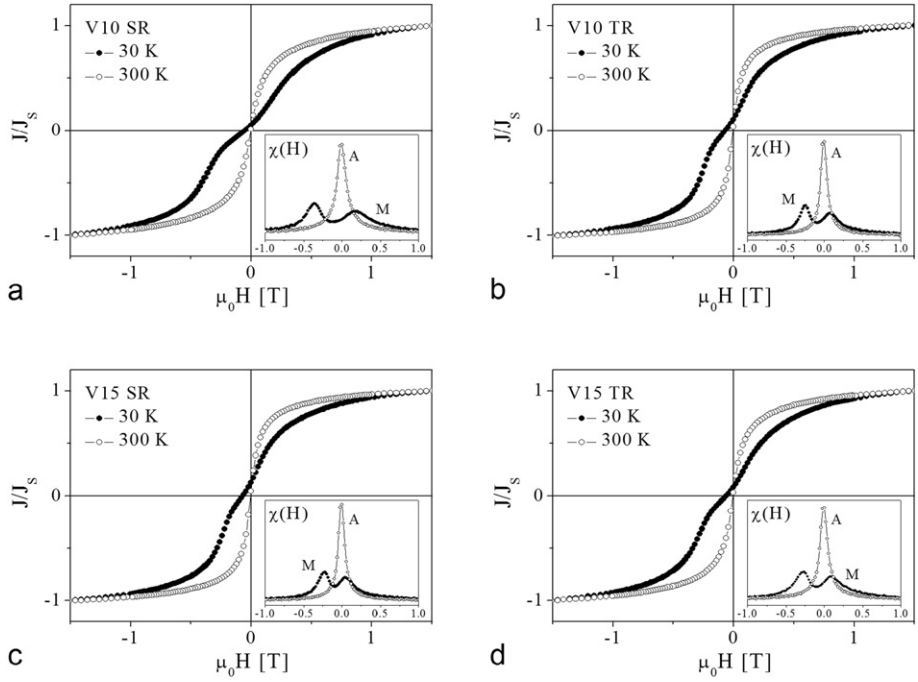

Fig. 12. Upper branch of the hysteresis loops measured at 30 K and 300 K. The loops corresponding to the samples in the martensitic phase show two steps, as illustrated by the χ curves in the insets.

Table 5
Critical fields $\mu_0{}_\chi H_C$ associated to the steps observed in the demagnetization curves of the martensitic phase at 30 K. The apparent coercive field (applied field corresponding to $J(\mu_0 H_C) = 0$) of samples at 30 K and 300 K are also quoted.

Sample	V10 SR	V10 TR	V15 SR	V15 TR
$\mu_0{}_\chi H_{C1}$ [mT]	180	80	40	100
$\mu_0{}_\chi H_{C2}$ [mT]	−362	−241	−221	−261
$\mu_0{}_J H_{C\ 30K}$ [mT]	−50	−66	−68	−59
$\mu_0{}_J H_{C\ 300K}$ [mT]	−2	−3	−4	−4

the rapid solidification process, composition inhomogeneities, ordering degree and to smaller grain size. This disorder enhances the resistance to the transformation and depresses the martensitic transformation temperature. At a given wheel speed, no significant differences are observed between the austenite start temperatures for SR and TR melt-spun samples, but they are clearly lower for the ribbons quenched at 10 m/s (SR and TR) in agreement with a larger disorder.

The transformation hysteresis, $A_f - M_S$, is similar in all the samples analyzed, with an average value of 34 ± 3 K. The equilibrium temperature is also higher in samples (SR and TR) cooled at wheel speed V15 than those processed at V10.

The magnitude of the Hopkinson effect, mainly related to residual microstresses and the easy axis distribution, is larger in TR melt-spun samples, along with the higher residual stress level expected in these ribbons, as compared to SR ones.

Finally, it may be concluded that both procedures, SR and TR melt spinning, provide similar microstructures favoring magnetization mechanisms involving magnetic field induced twin variants reorientation.

Acknowledgments

The authors thank the following Argentine public institutions: CONICET, SECyT-UNC (Project No. 05/B501) and SECyT-UNCu (Project No. 06/C488), for the financial support given to this work.

References

[1] K. Ullako, J.K. Huang, C. Kantner, R.C. O'Handley, V.V. Kokorin, Large magnetic-field-induced strains in Ni_2MnGa single crystals, Appl. Phys. Lett. 69 (13) (1996) 1966–1968.
[2] S.J. Murray, M. Marioni, S.M. Allen, R.C. O'Handley, T.A. Lograsso, 6% magnetic-field-induced strain by twin-boundary motion in ferromagnetic Ni-Mn-Ga, Appl. Phys. Lett. 77 (2000) 886–888.
[3] A. Sozinov, A.A. Likhachev, N. Lanska, K. Ullakko, Giant magnetic-field-induced strain in NiMnGa seven-layered martensitic phase, Appl. Phys. Lett. 80 (10) (2002) 1746–1748.
[4] Y. Zhang, M. Li, Y.D. Wang, J.P. Lin, K.A. Dahmen, Z.L. Wang, P.K. Liaw, Superelasticity and serration behavior in small-sized NiMnGa alloys, Adv. Eng. Mater. 16 (2014) 955–960.
[5] C. Biswas, R. Rawat, S.R. Barman, Large negative magnetoresistance in a ferromagnetic shape memory alloy: $Ni_{2+x}Mn_{1-x}Ga$, Appl. Phys. Lett. 86 (2005) 202508.
[6] S. Banik, S. Singh, R. Rawat, P.K. Mukhopadhyay, B.L. Ahuja, A.M. Awasthi, S.R. Barman, E.V. Sampathkumaran, Variation of magnetoresistance in $Ni_{2+x}Mn_{1-x}Ga$ with composition, J. Appl. Phys. 106 (2009) 103919.
[7] F.-X. Hu, B.-G. Shen, J.-R. Sun, G.-H. Wu, Large magnetic entropy change in a Heusler alloy $Ni_{52.6}Mn_{23.1}Ga_{24.3}$ single crystal, Phys. Rev. B 64 (2001) 132412.
[8] Z.B. Li, J.L. Sánchez Llamazares, C.F. Sánchez-Valdés, Y.D. Zhang, C. Esling, X. Zhao, L. Zuo, Microstructure and magnetocaloric effect of melt-spun $Ni_{52}Mn_{26}Ga_{22}$ ribbons, Appl. Phys. Lett. 100 (2012) 174102.
[9] Z. Li, Y. Zhang, C.F. Sánchez-Valdés, J.L. Sánchez Llamazares, C. Esling, X. Zhao, L. Zuo, Giant magnetocaloric effect in melt-spun Ni-Mn-Ga ribbons with magneto-multistructural transformation, Appl. Phys. Lett. 104 (2014) 044101.
[10] J. Marcos, A. Planes, L. Mañosa, F. Casanova, X. Batlle, A. Labarta, B. Martínez, Magnetic field induced entropy change and magnetoelasticity in Ni-Mn-Ga alloys, Phys. Rev. B 66 (2002) 224413.
[11] A. Planes, L. Mañosa, M. Acet, Magnetocaloric effect and its relation to shape-memory properties in ferromagnetic Heusler alloys, J. Phys. D. Appl. Phys. 21 (2009) 233201.
[12] R. Kainuma, Y. Imano, W. Ito, Y. Sutou, H. Morito, S. Okamoto, O. Kitakami, K. Oikawa, A. Fujita, T. Kanomata, K. Ishida, Magnetic-field-induced shape recovery by reverse phase transformation, Nature 439 (2006) 957–960.
[13] O. Heczko, A. Sozinov, K. Ullakko, Giant field-induced reversible strain in magnetic shape memory NiMnGa alloy, IEEE Trans. Magn. 36 (5) (2000) 3266–3268.
[14] O. Heczko, Magnetic shape memory effect and highly mobile twin boundaries, Mater. Sci. Technol. 30 (13a) (2014) 1559–1578.
[15] N.N. Stepanova, D.P. Rodionov, V.A. Kazantsev, V.A. Sazonova, Y.N. Akshentsev, Changes in the temperatures of phase transformations of the Ni_2MnGa alloy upon substitution of nickel for manganese, Phys. Met. Metallogr. 104 (6) (2007) 595–600.
[16] P.J. Webster, K.R.A. Ziebeck, S.L. Town, M.S. Peak, Magnetic order and phase transformation in Ni_2MnGa, Philos. Mag. B 49 (1984) 295–310.
[17] A.N. Vasil'ev, A.D. Bozhko, V.V. Khovailo, I.E. Dikshtein, V.G. Shavrov, V.D. Buchelnikov, M. Matsumoto, S. Suzuki, T. Takagi, J. Tani, Structural and magnetic phase transitions in shape-memory alloys $Ni_{2+x}Mn_{1-x}Ga$, Phys. Rev. B 59 (2) (1999) 1113–1120.
[18] V.A. Chernenko, J. Pons, C. Segui, E. Cesari, Premartensitic phenomena and other phase transformations in Ni-Mn-Ga alloys studied by dynamical mechanical analysis and electron diffraction, Acta Mater. 50 (2002) 53–60.
[19] J.I. Pérez-Landazábal, V. Sánchez-Alarcos, C. Gómez-Polo, V. Recarte, V.A. Chernenko, Vibrational and magnetic behavior of transforming and nontransforming Ni-Mn-Ga alloys, Phys. Rev. B 76 (2007) 092101.
[20] J. Pons, V.A. Chernenko, R. Santamarta, E. Cesari, Crystal structure of martensitic phases in Ni-Mn-Ga shape memory alloys, Acta Mater. 48 (2000) 3027–3038.
[21] D.Y. Cong, P. Zetterström, Y.D. Wang, R. Delaplane, R. Lin Peng, X. Zhao, L. Zuo, Crystal structure and phase transformation in $Ni_{53}Mn_{25}Ga_{22}$ shape memory alloy from 20 K to 473 K, Appl. Phys. Lett. 87 (2005) 111906.
[22] V.A. Chernenko, C. Segui, E. Cesari, J. Pons, V.V. Kokorin, Sequence of martensitic transformations in Ni-Mn-Ga alloys, Phys. Rev. B 57 (1998) 2659–2662.
[23] W.H. Wang, G.H. Wu, J.L. Chen, S.X. Gao, W.S. Zhan, G.H. Wen, X.X. Zhang, Intermartensitic transformation and magnetic-field-induced strain in $Ni_{52}Mn_{24.5}Ga_{23.5}$ single crystals, Appl. Phys. Lett. 79 (2001) 1148–1150.
[24] W.H. Wang, Z.H. Liu, J. Zhang, J.L. Chen, G.H. Wu, W.S. Zhan, T.S. Chin, G.H. Wen, X.X. Zhang, Thermoelastic intermartensitic transformation and its internal stress dependency in $Ni_{52}Mn_{24}Ga_{24}$ single crystals, Phys. Rev. B 66 (2002) 052411.
[25] Z. Li, B. Yang, Y. Zhang, C. Esling, N. Zou, X. Zhao, L. Zuo, Crystallographic insights into the intermartensitic transformation in Ni–Mn–Ga alloys, Acta Mater. 74 (2014) 9–17.
[26] L. Huang, D.Y. Cong, Z.L. Wang, Z.H. Nie, Y.H. Dong, Y. Zhang, Y. Ren, Y.D. Wang, Direct evidence for stress-induced transformation between coexisting multiple martensites in a Ni–Mn–Ga multifunctional alloy, J. Phys. D. Appl. Phys. 48 (2015) 265304.
[27] V.A. Chernenko, E. Cesari, J. Pons, C. Seguí, Phase transformations in rapidly quenched Ni-Mn-Ga alloys, J. Mater. Res. 15 (7) (2000) 1496–1504.
[28] V.A. Chernenko, M. Chmielus, P. Müllner, Large magnetic-field-induced strains in Ni–Mn–Ga nonmodulated martensite, Appl. Phys. Lett. 95 (2009) 104103.
[29] M. Pasquale, C. Sasso, S. Besseghini, F. Passaretti, E. Villa, A. Sciacca, NiMnGa polycrystalline magnetically activated shape memory alloys, IEEE Trans. Magn. 36 (5) (2000) 3263–3265.
[30] J. Wang, C. Jiang, R. Techapiesancharoenkij, D. Bono, S.M. Allen, R.C. O'Handley, Anomalous magnetizations in melt-spinning Ni–Mn–Ga, J. Appl. Phys. 106 (2009) 023923.
[31] O. Söderberg, I. Aaltio, Y. Ge, O. Heczko, S.-P. Hannula, Ni–Mn–Ga multifunctional compounds, Mater. Sci. Eng. A 481–482 (2008) 80–85.
[32] S. Guo, Y. Zhang, J. Li, B. Quan, Y. Qi, X. Wang, Martensitic transformation and magnetic-field-induced strain in magnetic shape memory alloy NiMnGa melt-spun ribbon, J. Mater. Sci. Technol. 21 (2005) 211–214.
[33] N.V. Rama Rao, R. Gopalan, M. Manivel Raja, J. AroutChelvane, B. Majumdar, V. Chandrasekaran, Magneto-structural transformation studies in melt-spun Ni–Mn–Ga ribbons, Scr. Mater. 56 (2007) 405–408.
[34] N.V. Rama Rao, R. Gopalan, V. Chandrasekaran, K.G. Suresh, Microstructure, magnetic properties and magnetocaloric effect in melt-spun Ni–Mn–Ga ribbons, J. Alloys Compd. 478 (2009) 59–62.
[35] J. Wang, C. Jiang, R. Techapiesancharoenkij, D. Bono, S.M. Allen, R.C. O'Handley, Microstructure and magnetic properties of melt-spinning Ni-Mn-Ga, Intermetallics 32 (2013) 151–155.
[36] G. Pozo-López, A.M. Condó, R.N. Giordano, S.E. Urreta, N. Haberkorn, E. Winkler, L.M. Fabietti, Microstructure and magnetic properties of as-cast Ni_2MnGa alloys processed by twin-roller melt spinning, J. Magn. Magn. Mater. 335 (2013) 75–85.
[37] A. Hadadzadeh, M.A. Wells, In-Ho Jung. Scale-up modeling of the twin roll casting process for AZ31 magnesium alloy, J. Manuf. Process. 16 (4) (2014) 468–478.
[38] B. Hernando, J.L. Sánchez Llamazares, J.D. Santos, M.L. Sánchez, L. Escoda, J.J. Suñol, R. Varga, C. García, J. González, Grain oriented NiMnSn and NiMnIn Heusler alloys ribbons produced by melt spinning: martensitic transformation and magnetic properties, J. Magn. Magn. Mater. 321 (2009) 763–768.
[39] Y. Takamura, R. Nakane, S. Sugahara, Analysis of $L2_1$-ordering in full-Heusler Co_2FeSi alloy thin films formed by rapid thermal annealing, J. Appl. Phys. 105 (2009) 07B109.
[40] C. Dong, F. Wu, H. Chen, Correction of zero shift in powder diffraction patterns using the reflection-pair method, J. Appl. Crystallogr. 32 (1999) 850–853.
[41] G.D. Serrano, J.L. Pelegrina, A.M. Condó, M. Ahlers, Helical dislocations as vacancy sinks in β phase Cu–Zn–Al–Ni alloys, Mater. Sci. Eng. A 433 (2006) 149–154.
[42] J.D. Robson, The effect of internal stresses due to precipitates on twin growth in magnesium, Acta Mater. 121 (2016) 277–287.
[43] T.B. Massalski, H. Okamoto, P.R. Subramanian, L. Kacprzak, second ed., Binary Alloy Phase Diagrams, vol. 3, ASM International, Materials Park, Ohio, 1990.
[44] M.F. Ashbv, L.M. Brown, Diffraction contrast from spherically symmetrical coherency strains, Philos. Mag. 8 (1963) 1083–1103.

[45] O. Söderberg, A. Sozinov, Y. Ge, S.-P. Hannula, V.K. Lindroos, Giant magnetostrictive materials, in: K.H.J. Buschow (Ed.), Handbook of Magnetic Materials, vol. 16, Elsevier B.V., Amsterdam, 2006.
[46] V.A. Chernenko, E. Cesari, J. Pons, C. Seguí, Phase transformations in rapidly quenched Ni-Mn-Ga alloys, J. Mater. Res. 15 (2000) 1496–1504.
[47] M. Matsumoto, M. Ohtsuka, K. Itagaki, T. Takagi, T. Fujino, Ferromagnetic shape memory alloy Ni_2MnGa films, J. Phys. IV France 11 (2001) (Pr8–275-279).
[48] F. Albertini, S. Besseghini, A. Paoluzi, L. Pareti, M. Pasquale, F. Passaretti, C.P. Sasso, A. Stantero, E. Villa, Structural, magnetic and anisotropic properties of Ni_2MnGa melt-spun ribbons, J. Magn. Magn. Mater. 242-245 (2002) 1421–1424.
[49] P. Machain, A.M. Condó, P. Domenichini, G. Pozo López, M. Sirena, V.F. Correa, N. Haberkorn, Martensitic transformation in as-grown and annealed near-stoichiometric epitaxial Ni_2MnGa thin films, Philos. Mag. 95 (23) (2015) 2527–2538.
[50] R.W. Overholser, M. Wuttig, D.A. Neumann, Chemical ordering in Ni-Mn-Ga Heusler alloys, Scr. Mater. 40 (1999) 1095–1102.
[51] V. Sánchez-Alarcos, V. Recarte, J.I. Pérez-Landazábal, G.J. Cuello, Correlation between atomic order and the characteristics of the structural and magnetic transformations in Ni–Mn–Ga shape memory alloys, Acta Mater. 55 (2007) 3883–3889.
[52] R. Santamarta, E. Cesari, J. Font, J. Muntasell, J. Pons, J. Dutkiewicz, Effect of atomic order on the martensitic transformation of Ni–Fe–Ga alloys, Scr. Mater. 54 (12) (2006) 1985–1989.
[53] L. Kaufman, M. Cohen, Thermodynamics and kinetics of martensitic transformations, in: B. Chalmers, R. King (Eds.), Progress in Metal Physics, 7, Pergamon Press, London 1958, p. 165.
[54] A. Planes, E. Obradó, A. Gonzàlez-Comas, L. Mañosa, Premartensitic transition driven by magnetoelastic interaction in bcc ferromagnetic Ni_2MnGa, Phys. Rev. Lett. 79 (1997) 3926–3929.
[55] P. Entel, V.D. Buchelnikov, M.E. Gruner, A. Hucht, V.V. Khovailo, S.K. Nayak, A.T. Zayak, Shape memory alloys: a summary of recent achievements, Mater. Sci. Forum 583 (2008) 21–41.
[56] A. Gonzàlez-Comas, E. Obradó, L. Mañosa, A. Planes, V.A. Chernenko, B.J. Hattink, A. Labarta, Premartensitic and martensitic phase transitions in ferromagnetic Ni_2MnGa, Phys. Rev. B 60 (10) (1999) 7085–7090.
[57] V. Sánchez-Alarcos, J.I. Pérez-Landazábal, V. Recarte, C. Gómez-Polo, V.A. Chernenko, Pre-martensitic phenomena in a near stoichiometric Ni_2MnGa polycrystalline alloy, Int. J. Appl. Electromagn. Mech. 23 (2006) 93–98.
[58] B.D. Cullity, C.D. Graham, Introduction to Magnetic Materials, second ed. IEEE Press, Piscataway, NJ, USA, 2009 323.
[59] J. Gutiérrez, J.M. Barandiarán, P. Lázpita, C. Seguí, E. Cesari, Magnetic properties of a rapidly quenched Ni–Mn–Ga shape memory alloy, Sensors Actuators A 129 (2006) 163–166.
[60] O. Heczko, Understanding motion of twin boundary—a key to magnetic shape memory effect, IEEE Trans. Magn. 50 (11) (2014) 2505807.
[61] O. Heczko, V. Kopecky, A. Sozinov, L. Straka, Magnetic shape memory effect at 1.7 K, Appl. Phys. Lett. 103 (2013) 072405.
[62] Z. Li, Y. Zhang, C. Esling, X. Zhao, L. Zuo, Twin relationships of 5 M modulated martensite in Ni–Mn–Ga alloy, Acta Mater. 59 (2011) 3390–3397.
[63] A. Pramanick, X.-L. Wang, A.D. Stoica, C. Yu, Y. Ren, S. Tang, Z. Gai, Kinetics of magnetoelastic twin-boundary motion in ferromagnetic shape-memory alloys, Phys. Rev. Lett. 112 (2014) 217205.
[64] D. Kellis, A. Smith, K. Ullakko, P. Müllner, Oriented single crystals of Ni–Mn–Ga with very low switching field, J. Cryst. Growth 359 (2012) 64–68.